EDGE ARTICLE

Check for updates

The spatial distribution of cobalt phthalocyanine and copper nanocubes controls the selectivity towards C₂ products in tandem electrocatalytic CO₂ reduction†

Min Wang,[a] Anna Loiudice,[b] Valery Okatenko,[a] Ian D. Sharp [ID][b] and Raffaella Buonsanti [ID] *[a]

The coupling of CO-generating molecular catalysts with copper electrodes in tandem schemes is a promising strategy to boost the formation of multi-carbon products in the electrocatalytic reduction of CO_2. While the spatial distribution of the two components is important, this aspect remains underexplored for molecular-based tandem systems. Herein, we address this knowledge gap by studying tandem catalysts comprising Co-phthalocyanine (CoPc) and Cu nanocubes (Cu_{cub}). In particular, we identify the importance of the relative spatial distribution of the two components on the performance of the tandem catalyst by preparing $CoPc-Cu_{cub}/C$, wherein the CoPc and Cu_{cub} share an interface, and $CoPc-C/Cu_{cub}$, wherein the CoPc is loaded first on carbon black (C) before mixing with the Cu_{cub}. The electrocatalytic measurements of these two catalysts show that the faradaic efficiency towards C_2 products almost doubles for the $CoPc-Cu_{cub}/C$, whereas it decreases by half for the $CoPc-C/Cu_{cub}$, compared to the Cu_{cub}/C. Our results highlight the importance of a direct contact between the CO-generating molecular catalyst and the Cu to promote C–C coupling, which hints at a surface transport mechanism of the CO intermediate between the two components of the tandem catalyst instead of a transfer *via* CO diffusion in the electrolyte followed by re-adsorption.

Introduction

The electrochemical CO_2 reduction reaction (CO_2RR) is an attractive route for CO_2 recycling, wherein value-added chemicals and fuels are produced from CO_2 while also storing electricity generated from renewable energy sources.[1,2] Among all catalysts, Cu-based materials provide suitable intermediate binding energies to drive CO_2RR towards highly reduced products (*e.g.* methane, ethylene, ethanol), which are of interest due to their high energy densities.[3,4] To date, tremendous effort has been dedicated to increasing the selectivity towards targeted products of the reaction, which produces over sixteen different products in various yields when performed over a polycrystalline Cu foil.[5]

Cu-based tandem schemes have emerged as a valid strategy to enhance the selectivity of CO_2RR towards multicarbon products (C_{2+}) by decoupling the CO_2 to CO and the CO to C_{2+} reduction steps.[6–9] Previous work has demonstrated that increasing the local

concentration of CO and/or the surface coverage of adsorbed CO (*CO) decreases the energetic barrier for C–C coupling, which is the rate-determining step towards C_{2+} products on Cu surfaces.[10–17] In addition to their intrinsic catalytic properties (*i.e.* turnover frequency, selectivity, overpotential), the relative spatial arrangement of the CO-producing component and of the Cu catalyst plays an important role in defining the efficiency of such tandem systems.[9,18–20] For example, researchers have synthesized reverse core–shell structures, with the CO-producing catalyst (Ag) in the core and the Cu as a shell, which was found to maximize CO utilization and enhance the C_{2+} activity compared to core–shell structures with Cu in the core.[19] In an alternative approach, similar benefit was obtained by rationally segmenting the Ag and Cu components in gas-diffusion electrodes.[20] In both cases, the spatial distribution of the two catalysts impacts the modality of CO transport to the active sites, which can occur either *via* surface diffusion or *via* sequential adsorption following transport through the gas phase or the electrolyte. Thus, optimization of the tandem catalyst configuration emerges as an important parameter to modulate the CO utilization efficiency.

Most studies on the design of tandem systems have so far focused on the coupling of Cu with a second metallic domain (Zn,[21,22] Au[23] or Ag[24–27]) as the CO-generating catalyst. Molecular catalysts, such as cobalt phthalocyanine[28] and iron

[a]Laboratory of Nanochemistry for Energy (LNCE), Institute of Chemical Sciences and Engineering (ISIC), École Polytechnique Fédérale de Lausanne, CH-1950 Sion, Switzerland. E-mail: raffaella.buonsanti@epfl.ch

[b]Walter Schottky Institute and Physics Department, Technische Universität München, Am Coulombwall 4, 85748 Garching, Germany

† Electronic supplementary information (ESI) available. See DOI: https://doi.org/10.1039/d2sc06359j

porphyrin[29,30] have also been successfully employed as the CO-generating catalyst in the context of tandem schemes. Compared to metals, molecular catalysts offer additional versatility for varying the local CO concentration and production rate thanks to the superior chemical tunability *via* synthetic modifications of molecules *versus* materials.[30] Despite their promise, no experimental work has investigated yet the influence of the spatial arrangement of the components on the catalytic performance of molecular-Cu based tandem systems.

In this work, we investigate the impact of a direct interface between the molecular catalyst and the Cu electrode on the C–C coupling efficiency. We use colloidally dispersible Cu nanocubes (Cu_{cub}) enclosed by (100) facets as model catalysts. Their high surface to volume ratio, which is ideal for exploring surface phenomena, as well as their intrinsic selectivity towards ethylene production, justify this choice.[31–33] To work alongside Cu_{cub}, we select cobalt phthalocyanine (CoPc) as the CO-producing molecular catalyst. In addition to being highly active and stable when immobilized on conductive substrates for CO_2RR, the reduction potential window matches the applied potentials of Cu_{cub} in aqueous solutions.[34–37] Additionally, CoPc readily adsorbs on different surfaces, including carbon and metallic Cu, *via* electrostatic interactions, thanks to the Pc planar structure.[38–40] Finally, both catalysts (*i.e.* the CoPc and the Cu_{cub}) can be produced in the form of inks, which facilitates the manipulation of their surface interactions. We exploit these intrinsic characteristics of the Cu_{cub} and of the CoPc to create tandem catalysts comprising $CoPc-Cu_{cub}/C$, where the CoPc shares a direct interface with the Cu_{cub}, and $CoPc-C/Cu_{cub}$, where the CoPc is first adsorbed on carbon black and then mixed with the Cu_{cub}. We find that the $CoPc-Cu_{cub}/C$ catalyst exhibits a faradaic efficiency (FE) and partial current density for C_2 products which are double the values measured for pristine Cu_{cub}/C without the molecular component present. In contrast, the FE for C_2 products decrease by half for the $CoPc-C/Cu_{cub}$ compared to the Cu_{cub}/C. These results demonstrate that CO utilization is much more efficient in the $CoPc-Cu_{cub}/C$, where a close contact between the two components of the tandem catalyst exists. Thus, we propose that surface transport, which requires a direct interface, dominates over electrolyte-mediated diffusion-readsorption and is the favorable pathway to maximize the CO utilization efficiency and C_2 product formation in these molecular-based tandem catalysts.
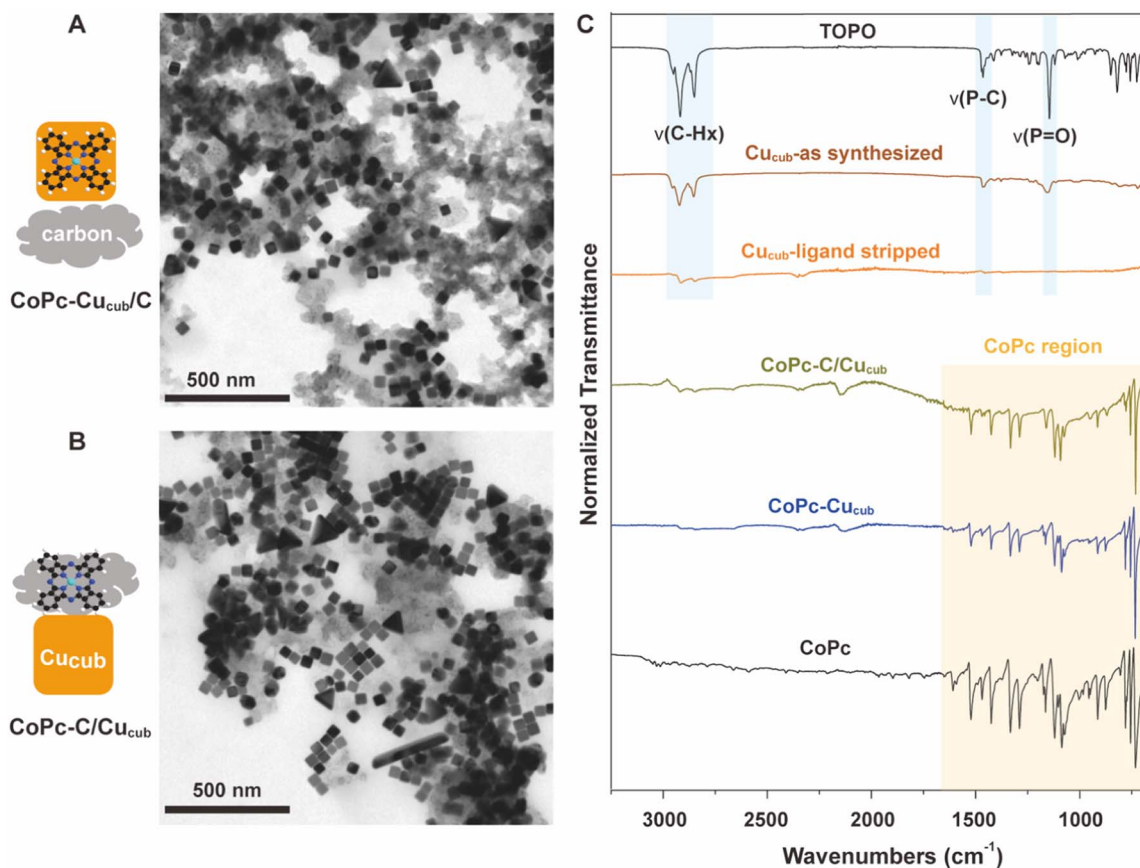

Fig. 1 (A and B) Bright field TEM images of $CoPc-Cu_{cub}/C$ (A) and $CoPc-C/Cu_{cub}$ (B), confirming that the structure of Cu_{cub} is retained in both cases following catalyst preparation. The synthesized tandem catalyst structures are schematically indicated on the left. (C) FTIR spectra of TOPO ligand, the as-synthesized Cu_{cub}, ligand-stripped Cu_{cub}, $CoPc-Cu_{cub}$, $CoPc-C/Cu_{cub}$ and CoPc. These results demonstrate the successful removal of TOPO ligand from Cu_{cub} and the retention of CoPc within both catalyst assemblies.

Results and discussion

The CoPc-Cu$_{cub}$/C catalyst was obtained by first mixing the CoPc molecules with the Cu$_{cub}$ in dimethylformamide (DMF), followed by the addition of carbon black into CoPc-Cu$_{cub}$. Prior to mixing, the native ligands of the Cu$_{cub}$ were removed *via* solvent washing, which allowed them to become dispersible in DMF. The molecular catalyst was added in excess to the washed Cu$_{cub}$ in order to maximize the Cu surface coverage (see Experimental section in ESI† for details). The amount of the adsorbed molecular catalyst (~1 nmol per cm^2 per working electrode) was quantified by inductively coupled plasma-optical emission spectrometry (ICP-OES) (Table S1†). The CoPc-C/Cu$_{cub}$ catalyst was prepared by adsorbing the same total amount of CoPc on the carbon black prior to mixing with the Cu$_{cub}$. For reference, carbon black was also added to the individual Cu$_{cub}$ and CoPc systems (Cu$_{cub}$/C and CoPc/C) to enable a direct comparison among each of the different systems.

Fig. 1 reports the transmission electron microscopy (TEM) and Fourier transform infrared spectroscopy (FTIR) characterization of the as-obtained catalysts. TEM reveals the intact cubic shape of the Cu$_{cub}$ in both CoPc-Cu$_{cub}$/C (Fig. 1A) and CoPc-C/Cu$_{cub}$ (Fig. 1B), which proves that the synthesis procedure does not impact the Cu$_{cub}$ morphology. The low contrast material in both images is the carbon black. The FTIR data presented in Fig. 1C show that, first of all, the washed Cu$_{cub}$ (Cu$_{cub}$–ligand stripped) has ligand-free surfaces. Indeed, the intensity of the –

CH– stretching at 2915 cm^{-1} is negligible compared to the as-synthesized sample and the P=O vibration is completely absent. Both vibrational modes are representative of the native trioctylphosphine oxide ligands of the Cu$_{cub}$ (area shaded in blue), confirming their removal from the Cu nanoparticles. The characteristic peaks of CoPc (area shaded in yellow: with Pc ring at 753 cm^{-1}, pyrrole C–N asymetric stretch at approximately 1086 cm^{-1}, and the isoindole and pyrrole stretch at 1200–1500 cm^{-1}) are present in the CoPc-Cu$_{cub}$ sample even after thoroughly washing, proving that the CoPc is strongly adsorbed on the Cu$_{cub}$ surface, likely due to the expected electrostatic interactions. Similarly, the characteristic IR peaks of CoPc are present for the CoPc-C/Cu$_{cub}$ catalyst. The background signal in the region from 700 cm^{-1} to 2000 cm^{-1}, is attributed to the carbon black (Fig. S1†).

We further characterized the catalysts by high-angle annular dark field scanning transmission electron microscopy (HAADF-STEM) coupled with energy-dispersive X-ray (EDX) spectroscopy to learn more about the spatial distributions of the different components (Fig. 2). For the case of the CoPc-Cu$_{cub}$ catalyst, the Cu and Co signals are co-localized on the Cu$_{cub}$ and no free CoPc molecules are present on the grid (Fig. 2A and B). By contrast, for the case of CoPc-C/Cu$_{cub}$ catalyst, the CoPc is present only on the carbon black and not on the Cu$_{cub}$ (Fig. 2C and D). These results confirm the successful assembly of two different catalyst motifs according to the designed structures depicted by the schematic illustrations in Fig. 1A.
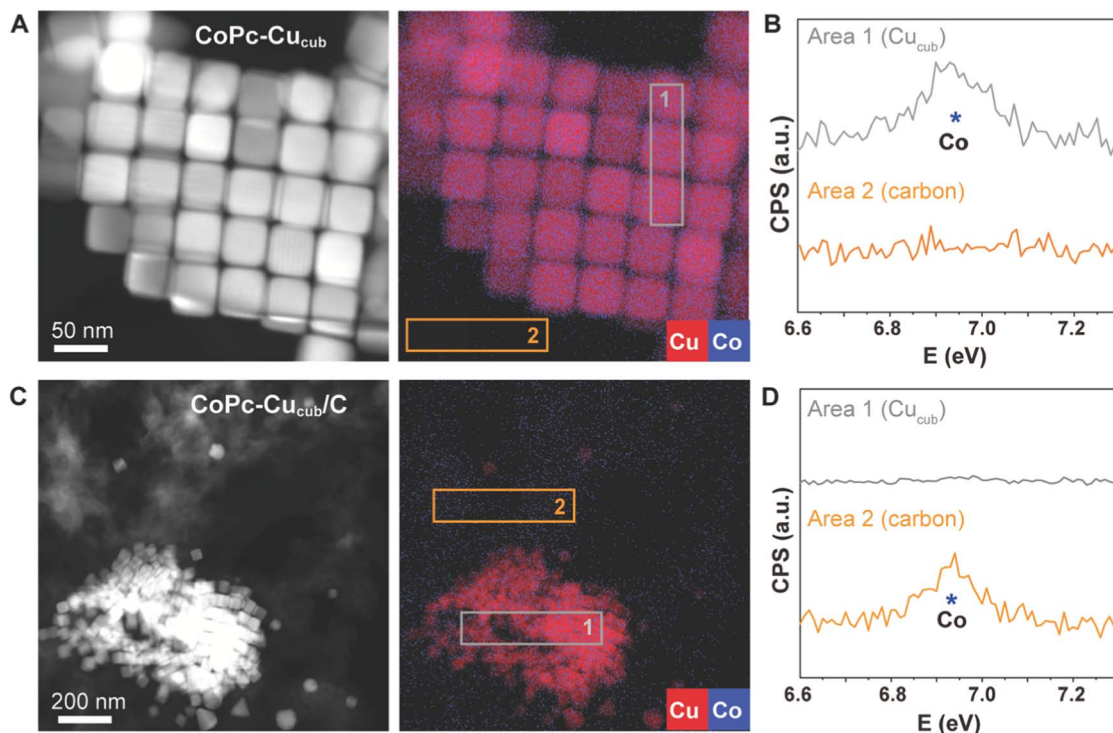

Fig. 2 (A and C) HAADF–STEM images and corresponding EDX elemental maps, along with (B and D) EDX spectra for CoPc–Cu$_{cub}$/C (A and B) and CoPc–C/Cu$_{cub}$ (C and D). The EDX maps show the spatial distributions of Cu (red) and Co (blue). The carbon is the low contrast material in (C) and is not colored for the sake of clarity. The EDX spectra report the intensity of the Co signals in two different areas of the map, which correspond to the Cu$_{cub}$ (area 1) and to the carbon (area 2), as indicated on the colored maps.
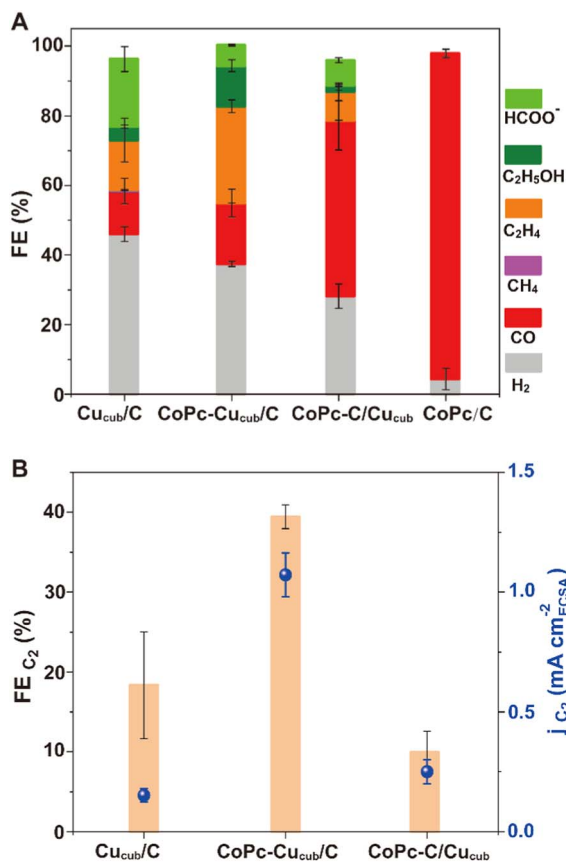
Fig. 3 (A) FEs for all gaseous products (*i.e.*, H_2, CO, CH_4, C_2H_4) and the main liquid products (*i.e.*, formate, C_2H_5OH), (B) FE_{C_2} and corresponding partial current density j_{C_2} normalized by the ECSA for the Cu_{cub}/C, CoPc-Cu_{cub}/C, CoPc-C/Cu_{cub} and CoPc/C. The loading of Cu_{cub} was 20 μg cm^{-2} and the loading of CoPc anchored on the Cu_{cub} and on the carbon black was 1.1 nmol cm^{-2} and 0.9 nmol cm^{-2}, respectively. These data were collected in an H-cell configuration using 0.1 M $KHCO_3$ as the electrolyte with the working electrode poised at −1.0 V *vs.* RHE for 1 h. The reported values are an average of three independent experiments with error bars indicating the standard deviations. Compared to the reference Cu_{cub}/C, a significant increase of FE_{C_2} is observed for CoPc-Cu_{cub}/C, while a decrease is observed for CoPc-C/Cu_{cub}.

Having completed the characterization of the two catalysts, we evaluated the behavior of CoPc-Cu_{cub}/C and CoPc-C/Cu_{cub} towards CO_2RR in a H-cell system, using CO_2-saturated 0.1 M aqueous $KHCO_3$ as the supporting electrolyte (Fig. 3). We chose an electrochemical potential of −1.0 V *vs.* RHE (reversible hydrogen electrode) for initial comparison based on the previous knowledge that Cu_{cub} exhibits a significant selectivity for C_2H_4 and that CoPc possesses maximum activity for CO near this working potential. For reference, the product distributions for the tandem catalyst assemblies are also compared to those possessing only the individual components, Cu_{cub}/C and CoPc/C. All reported current densities are normalized by the electrochemically active surface area (ECSA) (Fig. S2†).

The product distribution analysis (Fig. 3A), which is represented by the FE values, reveals that the major products observed for Cu_{cub}/C are still present for the CoPc-Cu_{cub}/C, but

with a clear increase of the FE for C_2 products (*i.e.* ethylene + ethanol). However, for the CoPc-C/Cu_{cub}, CO production notably increases while the other products are suppressed. Importantly, FE_{H_2} is suppressed for both CoPc-Cu_{cub}/C and CoPc-C/Cu_{cub} compared to the Cu_{cub}/C. As expected, the major product for CoPc/C is CO, with minor production of H_2, indicating that the activity of the heterogenized molecular component is preserved.

To facilitate the comparison of C_2 products, Fig. 3B reports the FE_{C_2} and the corresponding partial current densities (j_{C_2}) of all Cu_{cub}-based systems. The CoPc-Cu_{cub}/C clearly shows an enhancement of C_2 products with the highest FE of 39.4% and j_{C_2} of 1.07 mA cm^{-2}. In contrast, the FE_{C_2} for CoPc-C/Cu_{cub} is only 10%, much lower than that of the Cu_{cub}/C, which is 18.3%. The j_{C_2} are instead comparable and equal to 0.2 mA cm^{-2} for CoPc-C/Cu_{cub} and 0.16 mA cm^{-2} for the Cu_{cub}.

The high FE_{CO} and the suppressed FE_{C_2} for CoPc-C/Cu_{cub} suggests that CO released from the molecule diffuses away rather than being utilized by the Cu_{cub}. Longer reaction times up to 10 hours do eventually result in a slight increase of FE_{C_2} and j_{C_2} for CoPc-C/Cu_{cub} (Fig. S3†), which might result from the overall increasing concentration of CO in the electrolyte. However, the performance of CoPc-C/Cu_{cub} remain always lower than CoPc-Cu_{cub}/C and Cu_{cub}/C. Decreasing the loading of the CoPc does decrease the FE_{CO} but does not improve the FE_{C_2} compared to CoPc-Cu_{cub}/C with same CoPc loading and to Cu_{cub}/C (Fig. S4†), which indicates that the CO transfer from CoPc-C to Cu_{cub} does not efficiently occur in these catalysts.

To further investigate the mechanism behind the observed catalytic activity differences, we investigated the CoPc-Cu_{cub}/C and CoPc-C/Cu_{cub} CO_2RR performance over a wide range of applied potentials and compared them to those of Cu_{cub}/C and CoPc/C (Fig. 4). We note that the CoPc stability decreases and the selectivity for methane increases at more negative voltages (Fig. S5†). Consistent with the data in Fig. 3, CoPc-Cu_{cub}/C exhibits a similar potential-dependent product distribution compared to Cu_{cub}/C, but with an increased C_2 product yield and suppressed hydrogen generation across the entire potential range (Fig. 4A). In particular, the FE_{C_2} and the corresponding partial current density of the CoPc-Cu_{cub}/C are consistently higher than the values measured for the Cu_{cub}/C and increase at more cathodic potentials (Fig. 4B). The best-performing CoPc-Cu_{cub}/C possess a FE_{C_2} of 48% with a partial current density of 1.5 mA cm^{-2} at −1.05 V *vs.* RHE, which is 1.7 times the FE_{C_2} of the Cu_{cub}/C. In contrast, for the CoPc-C/Cu_{cub} assembly, CO is the major product and the FE_{C_2} is reduced over the whole potential range compared to Cu_{cub}/C (Fig. 4D). Furthermore, the partial current density of the C_2 products in CoPc-C/Cu_{cub} and Cu_{cub}/C is always similar, which indicates that the Cu_{cub} intrinsic selectivity is unaffected by the CoPc molecules (Fig. 4D). We also note that the total current densities of the tandem catalysts are higher compared to those of either the Cu_{cub} or the CoPc alone (Fig. S8†), which indicates that both components are active (Fig. S8†). Furthermore, the overall C_2 production rate is higher in the tandem catalysts compared to the Cu_{cub} alone (Fig. S8†), which is similar to what has been reported for some of the metallic/Cu tandem catalysts.[41,42] We highlight that
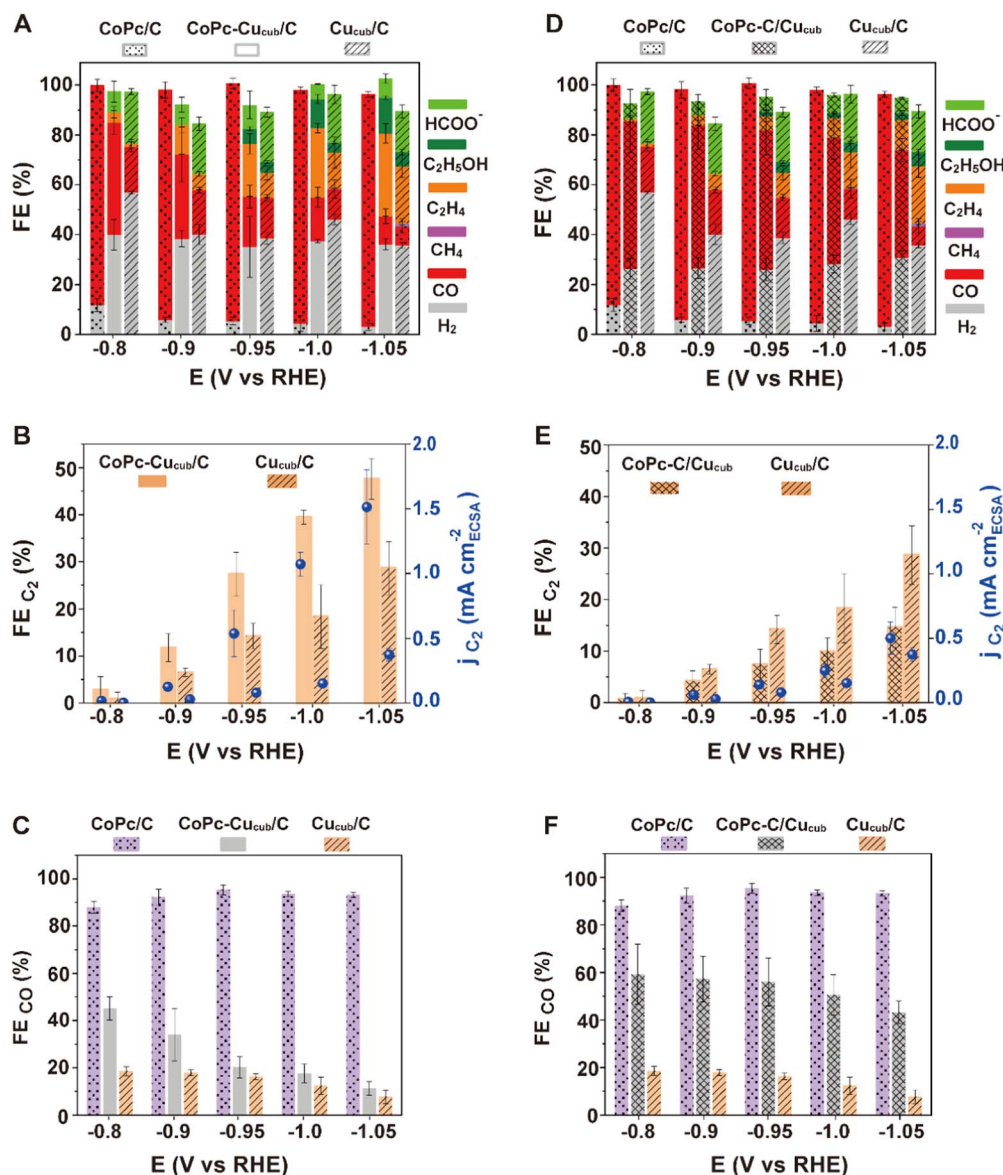
Fig. 4 (A and D) FEs for all gaseous products (*i.e.*, H_2, CO, CH_4, C_2H_4) and the main liquid products (*i.e.*, formate, C_2H_5OH), (B and E) FEs and partial current densities of C_2 products (*i.e.* $C_2H_4 + C_2H_5OH$), j_{C_2}, normalized by the ECSA and (C and F) FEs for CO as a function of potential for Cu_{cub}/C, CoPc-Cu_{cub}/C, CoPc-C/Cu_{cub} and CoPc/C. The loading of Cu_{cub} was 20 μg cm^{-2} and the loading of CoPc anchored on the Cu_{cub} and on the carbon black was 1.1 nmol cm^{-2} and 0.9 nmol cm^{-2}, respectively. These data were collected in a H-cell system using 0.1 M $KHCO_3$ as the electrolyte for 1 h. The reported values are an average of three independent experiments with error bars indicating the standard deviations.

morphology and composition of all catalysts were maintained after CO_2RR at −1.05 V *vs.* RHE for 1 hour (Fig. S6†).

To understand whether the C–C coupling enhancement in the CoPc-Cu_{cub}/C catalyst is consistent with a tandem mechanism, we plotted the FE_{CO} of the different systems at various electrochemical potentials (Fig. 4C and F). The FE_{CO} for the CoPc-Cu_{cub}/C decreases as the potential becomes more cathodic (Fig. 4C), concomitant with the C_2 production increase. This correlation is consistent with a tandem mechanism in which the CO formed on CoPc is consumed by Cu_{cub}. By contrast, the FE_{CO} of the CoPc-C/Cu_{cub} catalyst remains approximately constant and is similar to that of CoPc/C across the entire potential range (Fig. 4F), proving that the CO formed on CoPc is

not consumed by Cu_{cub} and the sequential tandem reaction does not occur.

To further validate the conclusion that the obtained results are due to a tandem effect, we performed control experiments to investigate whether other factors could be involved. XPS revealed that the electronic properties of the catalysts are not impacted by interactions between the different components and are, therefore, not responsible for the observed catalytic differences (Fig. S8 and Table S2†). In addition, we verified that neither the phthalocyanine ligand nor the Co alone on the Cu surface can provide the enhanced C–C coupling observed for CoPc-Cu_{cub}/C (Fig. S9–S11†). Finally, no major changes in hydrophobicity, which could justify hydrogen suppression, were observed upon
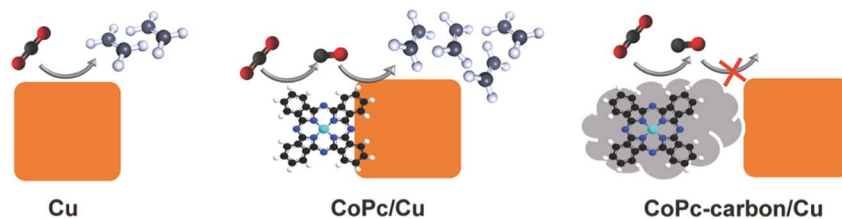
Fig. 5 Schematic illustration summarizing the effect of the spatial distribution of CO-producing molecular catalysts and Cu catalysts in tandem systems. The close spatial coupling and direct interface between the two components is crucial for enhancing C–C coupling *via* enhanced CO generation in the vicinity of Cu.

adsorption of the CoPc on the Cu_{cub} (Fig. S12†). Overall, the tandem effect emerges as the main reason underlying the C–C coupling enhancement observed in the CoPc-Cu_{cub}/C catalysts. Finally, encouraged by the results measured in a H-cell configuration, we included the spatial configured systems into a gas-fed flow cell, comprising the CoPc-Cu_{cub}/C and the CoPc-C/Cu_{cub} supported on a gas diffusion electrode as the cathode, in order to realize CO_2 to C_2 conversion at high current density (Fig. S13†). In agreement with the data discussed above, the CoPc-Cu_{cub}/C catalyst demonstrated enhanced C_2 production compared to the Cu_{cub}/C reaching a FE for C_2 of 62% with a partial current density of 125 mA cm^{-2} in 1 M KHCO$_3$.

Fig. 5 summarizes the results of this study and the proposed mechanism responsible for the observed electrocatalytic activity of molecule-copper tandem catalysts. We find that the close vicinity and direct interface between the CO-generating molecules and the Cu surface is essential to promote C–C coupling *via* the tandem effect. When the molecular component is spatially separated from the copper, the sequential tandem process does not occur and the overall multicarbon production is suppressed. These results suggest that the tandem mechanism in these catalysts is enabled by surface diffusion of the CO rather than CO diffusion in the electrolyte and sequential reabsorption.

Conclusions

In summary, we have demonstrated that tandem catalysts must be carefully engineered to promote efficient C–C coupling. In particular, our results reveal that a direct interface between the CO-generating molecular catalyst and the Cu is a key factor for efficient CO utilization by the copper. Indeed, we have reported a CO_2-to-C_2 conversion with FE of 48% at −1.05 V *vs.* RHE for CoPc-Cu_{cub}/C catalysts, which is 1.7 times higher than that of the Cu_{cub}/C when tested under the same conditions. In contrast, the CoPc-C/Cu_{cub} assembly, in which the Cu_{cub} and the CoPc were physically separated, exhibited a dramatically reduced FE_{C_2} compared to the Cu_{cub}. Overall, these findings advance our fundamental understanding of the performance-driving parameters necessary for constructing more efficient hybrid molecule/nanocrystal tandem catalysts in the future. For example, the discovery that a close spatial coupling is crucial for efficient tandem catalysts suggests that their integration into gas diffusion electrodes operating at high current density may

benefit from functional groups to anchor the molecular catalysts on the surface of the nanocatalysts.

Data availability

Data for this paper, including TEM images, FT-IR, HAADF-STEM images and corresponding EDX and electrochemical characterization, are available at Zenodo at: **https://doi.org/10.5281/zenodo.7327628**.

Author contributions

M. W. carried out the synthesis of the tandem catalysts and electrocatalytic testing for CO$_2$RR. A. L. performed X-ray photoelectron spectroscopy, HAADF-STEM images and corresponding EDX and contributed to daily discussions. V. O. and I. D. S. contributed to discussions. R. B. supervised this work and coordinated the project. All the authors contributed to the writing of the manuscript.

Conflicts of interest

There are no conflicts to declare.

References

1 G. Centi and S. Perathoner, Opportunities and prospects in the chemical recycling of carbon dioxide to fuels, *Catal. Today*, 2009, **148**(3–4), 191–205.

2 D. T. Whipple and P. J. A. Kenis, Prospects of CO$_2$ utilization via direct heterogeneous electrochemical reduction, *J. Phys. Chem. Lett.*, 2010, **1**(24), 3451–3458.

3 H.-R. M. Jhong, S. Ma and P. J. A. Kenis, Electrochemical conversion of CO$_2$ to useful chemicals: Current status, remaining challenges, and future opportunities, *Curr. Opin. Chem. Eng.*, 2013, **2**, 191–199.

4 Y. Y. Birdja, E. Pérez-Gallent, M. C. Figueiredo, A. J. Göttle, F. Calle-Vallejo and M. Koper, Advances and challenges in understanding the electrocatalytic conversion of carbon dioxide to fuels, *Nat. Energy*, 2019, **4**(9), 732–745.

5 S. Nitopi, E. Bertheussen, S. B. Scott, X. Liu, A. K. Engstfeld, S. Horch, B. Seger, I. E. L. Stephens, K. Chan, C. Hahn, J. K. Nørskov, T. F. Jaramillo and I. Chorkendorff, Progress and perspectives of electrochemical CO_2 reduction on copper in aqueous electrolyte, *Chem. Rev.*, 2019, **119**, 7610–7672.

6 Y. Lum and J. W. Ager, Sequential catalysis controls selectivity in electrochemical CO_2 reduction on Cu, *Energy Environ. Sci.*, 2018, **11**(10), 2935–2944.

7 A. Ozden, Y. Wang, F. Li, M. Luo, J. Sisler, A. Thevenon, D. Sinton, *et al.*, Cascade CO_2 electroreduction enables efficient carbonate-free production of ethylene, *Joule*, 2021, **5**(3), 706–719.

8 Y. Zhu, X. Cui, H. Liu, Z. Guo, Y. Dang, Z. Fan, W. Hu, *et al.*, Tandem catalysis in electrochemical CO_2 reduction reaction, *Nano Res.*, 2021, **14**, 4471–4486.

9 B. Cao, F. Z. Li and J. Gu, Designing Cu-Based Tandem Catalysts for CO_2 Electroreduction Based on Mass Transport of CO Intermediate, *ACS Catal.*, 2022, **12**, 9735–9752.

10 X. Wang, J. F. de Araújo, W. Ju, P. Strasser, *et al.*, Mechanistic reaction pathways of enhanced ethylene yields during electroreduction of CO_2-CO co-feeds on Cu and Cu-tandem electrocatalysts, *Nat. Nanotechnol.*, 2019, **14**, 1063–1070.

11 A. A. Peterson, F. Abild-Pedersen, F. Studt, J. Rossmeisl and J. K. Nørskov, How copper catalyzes the electroreduction of carbon dioxide into hydrocarbon fuels, *Energy Environ. Sci.*, 2010, **3**, 1311–1315.

12 A. J. Garza, A. T. Bell and M. Head-Gordon, Mechanism of CO_2 reduction at copper surfaces: pathways to C_2 products, *ACS Catal.*, 2018, **8**(2), 1490–1499.

13 T. K. Todorova, M. W. Schreiber and M. Fontecave, Mechanistic understanding of CO_2 reduction reaction (CO_2RR) toward multicarbon products by heterogeneous copper-based catalysts, *ACS Catal.*, 2020, **10**, 1754–1768.

14 J. Li, Z. Wang, C. McCallum, Y. Xu, F. Li, Y. Wang, D. Sinton, *et al.*, Constraining CO coverage on copper promotes high-efficiency ethylene electroproduction, *Nat. Catal.*, 2019, **2**(12), 1124–1131.

15 S. Louisia, D. Kim, Y. Li, M. Gao, S. Yu, I. Roh and P. Yang, The presence and role of the intermediary CO reservoir in heterogeneous electroreduction of CO_2, *Proc. Natl. Acad. Sci.*, 2022, **119**(18), e2201922119.

16 Y. Huang, A. D. Handoko, P. Hirunsit and B. S. Yeo, Electrochemical Reduction of CO_2 Using Copper Single-Crystal Surfaces: Effects of CO* Coverage on the Selective Formation of Ethylene, *ACS Catal.*, 2017, **7**, 1749–1756.

17 J. Gao, H. Zhang, X. Guo, J. Luo, S. M. Zakeeruddin, D. Ren and M. Grätzel, Selective C-C coupling in carbon dioxide electroreduction via efficient spillover of intermediates as supported by operando Raman spectroscopy, *J. Am. Chem. Soc.*, 2019, **141**(47), 18704–18714.

18 P. B. O'Mara, P. Wilde, T. M. Benedetti, C. Andronescu, S. Cheong, J. J. Gooding, R. D. Tilley and W. Schuhmann, Cascade Reactions in Nanozymes: Spatially Separated Active Sites inside Ag-Core–Porous-Cu-Shell Nanoparticles

for Multistep Carbon Dioxide Reduction to Higher Organic Molecules, *J. Am. Chem. Soc.*, 2019, **141**(36), 14093–14097.

19 L. Xiong, X. Zhang, L. Chen, Z. Deng, S. Han, Y. Chen, Y. Peng, *et al.*, Geometric Modulation of Local CO Flux in Ag@Cu_2O Nanoreactors for Steering the CO_2RR Pathway toward High-Efficacy Methane Production, *Adv. Mater.*, 2021, **33**(32), 2101741.

20 T. Zhang, J. C. Bui, Z. Li, A. T. Bell, A. Z. Weber and J. Wu, Highly selective and productive reduction of carbon dioxide to multicarbon products via in situ CO management using segmented tandem electrodes, *Nat. Catal.*, 2022, **5**(3), 202–211.

21 S. B. Varandili, D. Stoian, J. Vavra, K. Rossi, J. R. Pankhurst, Y. T. Guntern, L. Núria and R. Buonsanti, Elucidating the structure-dependent selectivity of CuZn towards methane and ethanol in CO_2 electroreduction using tailored Cu/ZnO precatalysts, *Chem. Sci.*, 2021, **12**(43), 14484–14493.

22 D. Ren, J. Gao, L. Pan, Z. Wang, J. Luo, S. M. Zakeeruddin, A. Hagfeldt and M. Grätzel, Atomic Layer Deposition of ZnO on CuO Enables Selective and Efficient Electroreduction of Carbon Dioxide to Liquid Fuels, *Angew. Chem., Int. Ed.*, 2019, **131**, 15178–15182.

23 C. G. Morales-Guio, E. R. Cave, S. A. Nitopi, J. T. Feaster, L. Wang, K. P. Kuhl, A. Jackson, N. C. Johnson, D. N. Abram, T. Hatsukade, C. Hahn and T. F. Jaramillo, Improved CO_2 reduction activity towards C_{2+} alcohols on a tandem gold on copper electrocatalyst, *Nat. Catal.*, 2018, **1**, 764–771.

24 Y. C. Li, Z. Wang, T. Yuan, D.-H. Nam, M. Luo, J. Wicks, B. Chen, J. Li, F. Li, F. P. G. de Arquer, Y. Wang, C.-T. Dinh, O. Voznyy, D. Sinton and E. H. Sargent, Binding site diversity promotes CO_2 electroreduction to ethanol, *J. Am. Chem. Soc.*, 2019, **141**, 8584–8591.

25 C. Chen, Y. Li, S. Yu, S. Louisia, J. Jin, M. Li, M. B. Ross and P. Yang, Cu-Ag Tandem Catalysts for High-Rate CO_2 Electrolysis toward Multicarbons, *Joule*, 2020, **4**, 1688–1699.

26 P. Iyengar, M. J. Kolb, J. R. Pankhurst, F. Calle-Vallejo and R. Buonsanti, Elucidating the facet-dependent selectivity for CO_2 electroreduction to ethanol of Cu-Ag tandem catalysts, *ACS Catal.*, 2021, **11**(8), 4456–4463.

27 J. Huang, M. Mensi, E. Oveisi, V. Mantella and R. Buonsanti, Structural sensitivities in bimetallic catalysts for electrochemical CO_2 reduction revealed by Ag-Cu nanodimers, *J. Am. Chem. Soc.*, 2019, **141**, 2490–2499.

28 X. Kong, J. Zhao, J. Ke, C. Wang, S. Li, R. Si, B. Liu, J. Zeng and Z. Geng, Understanding the Effect of *CO Coverage on C–C Coupling toward CO_2 Electroreduction, *Nano Lett.*, 2022, **22**(9), 3801–3808.

29 F. Li, Y. C. Li, Z. Wang, J. Li, D. H. Nam, Y. Lum and E. H. Sargent, Cooperative CO_2-to-ethanol conversion via enriched intermediates at molecule–metal catalyst interfaces, *Nat. Catal.*, 2020, **3**(1), 75–82.

30 M. Wang, V. Nikolaou, A. Loiudice, I. D. Sharp, A. Llobet and R. Buonsanti, Tandem electrocatalytic CO_2 reduction with Fe-porphyrins and Cu nanocubes enhances ethylene production, *Chem. Sci.*, 2022, **13**, 12673–12680.

31 A. Loiudice, P. Lobaccaro, E. A. Kamali, T. Thao, B. H. Huang, J. W. Ager and R. Buonsanti, Tailoring copper nanocrystals towards C_2 products in electrochemical CO_2 reduction, *Angew. Chem., Int. Ed.*, 2016, **55**, 5789–5792.

32 G. L. De Gregorio, T. Burdyny, A. Loiudice, P. Iyengar, W. A. Smith and R. Buonsanti, Facet-dependent selectivity of Cu catalysts in electrochemical CO_2 reduction at commercially viable current densities, *ACS Catal.*, 2020, **10**, 4854–4862.

33 D. Gao, I. Zegkinoglou, N. J. Divins, F. Scholten, I. Sinev, P. Grosse and B. Roldan Cuenya, Plasma-activated copper nanocube catalysts for efficient carbon dioxide electroreduction to hydrocarbons and alcohols, *ACS Nano*, 2017, **11**(5), 4825–4831.

34 Y. Wu, Y. Liang and H. Wang, Heterogeneous Molecular catalysts of metal phthalocyanines for electrochemical CO_2 reduction reactions, *Acc. Chem. Res.*, 2021, **54**(16), 3149–3159.

35 X. Zhang, Z. Wu, X. Zhang, L. Li, Y. Li, H. Xu, H. Wang, *et al.*, Highly selective and active CO_2 reduction electrocatalysts based on cobalt phthalocyanine/carbon nanotube hybrid structures, *Nat. Commun.*, 2017, **8**(1), 1–8.

36 S. Ren, D. Joulié, D. Salvatore, K. Torbensen, M. Wang, M. Robert and C. P. Berlinguette, Molecular electrocatalysts can mediate fast, selective CO_2 reduction in a flow cell, *Science*, 2019, **365**(6451), 367–369.

37 M. Wang, K. Torbensen, D. Salvatore, S. Ren, D. Joulié, F. Dumoulin, C. P. Berlinguette, M. Robert, *et al.*, CO_2 electrochemical catalytic reduction with a highly active cobalt phthalocyanine, *Nat. Commun.*, 2019, **10**(1), 1–8.

38 W. Auwärter, D. Écija, F. Klappenberger and J. V. Barth, Porphyrins at interfaces, *Nat. Chem.*, 2015, **7**(2), 105–120.

39 K. Shen, B. Narsu, G. Ji, H. Sun, J. Hu, Z. Liang, F. Song, *et al.*, On-surface manipulation of atom substitution between cobalt phthalocyanine and the Cu (111) substrate, *RSC Adv.*, 2017, **7**(23), 13827–13835.

40 A. Belser, K. Greulich, P. Grüninger, R. Karstens, R. Ovsyannikov, E. Giangrisostomi, H. Peisert, *et al.*, Perfluorinated Phthalocyanines on Cu(110) and Cu(110)-(2×1)O: The Special Role of the Central Cobalt Atom, *J. Phys. Chem. C*, 2021, **125**(16), 8803–8814.

41 T. T. Hoang, S. Verma, S. Ma, T. T. Fister, J. Timoshenko, A. I. Frenkel, A. A. Gewirth, *et al.*, Nanoporous copper–silver alloys by additive-controlled electrodeposition for the selective electroreduction of CO_2 to ethylene and ethanol, *J. Am. Chem. Soc.*, 2018, **140**(17), 5791–5797.

42 L. R. L. Ting, O. Pique, S. Y. Lim, M. Tanhaei, F. Calle-Vallejo and B. S. Yeo, Enhancing CO_2 electroreduction to ethanol on copper–silver composites by opening an alternative catalytic pathway, *ACS Catal.*, 2020, **10**(7), 4059–4069.